Electronic Supplementary Information (ESI)

Promoted Oxygen Reduction Kinetics on Nitrogen-doped Hierarchically Porous Carbon by Engineering Proton-feeding Centers

Guangbo Chen,[a]‡ Tao Wang,[b]‡ Pan Liu,[c] Zhongquan Liao,[d] Haixia Zhong,[a] Gang Wang,[a] Panpan Zhang,[a] Minghao Yu,[a] Ehrenfried Zschech,[d] Mingwei Chen,[e] Jian Zhang,*[f] and Xinliang Feng*[a]

[a] *Center for Advancing Electronics Dresden (Cfaed) and Faculty of Chemistry and Food Chemistry, Technische Universität Dresden, 01062 Dresden, Germany.*
E-mail: xinliang.feng@tu-dresden.de

[b] *SUNCAT Center for Interface Science and Catalysis, Department of Chemical Engineering, Stanford University, Stanford, CA 94305, USA.*

[c] *School of Chemistry and Chemical Engineering, Shanghai Jiao Tong University, 200230 Shanghai, P. R. China.*

[d] *Fraunhofer Institute for Ceramic, Technologies and Systems (IKTS), 01109 Dresden, Germany.*

[e] *Department of Materials Science and Engineering, Johns Hopkins University, Baltimore, MD 21218, USA.*

[f] *Department of Applied Chemistry, School of Applied and Natural Sciences, Northwestern Polytechnical University, Xi' an, 710129 P. R. China.*
E-mail: zhangjian@nwpu.edu.cn

‡ These authors contributed equally to this work.

Table of Contents:

Chemicals:

$Zn(NO_3)_3 \cdot 6H_2O$, 2-methylimidazole, phosphomolybdic acid (Mo12), Nafion perfluorinated resin solution (5 wt. % in mixture of lower aliphatic alcohols and water, contains 45% water) were obtained from Sigma-Aldrich. KOH and methanol were purchased from VWR chemicals. Pt/C (20%) was purchased from FuelCellStore. All the reagents were of analytical grade and used as received without further purification. Deionized water was used throughout the experimental processes.

Synthesis of α-MoC/NHPC and NHPC catalysts:

The α-MoC/NHPC electrocatalyst was synthesized by using a NaCl-assisted pyrolysis of Mo12/ZIF-8 precursors. First, the Mo12/ZIF-8 was prepared *via* co-precipitation of $Zn(NO_3)_2 \cdot 6H_2O$ (2.97 g), 2-methylimidazole (3.28 g) in a methanol solution (160 mL) containing phosphomolybdic acid (Mo12, 60 mg) at room temperature for 24 h. Second, the achieved Mo12/ZIF-8 (100 mg) was physically mixed with NaCl (35 mg) and then heated at 900 °C for 2 hours under nitrogen atmosphere. After washing and drying, α-MoC/NHPC with an α-MoC loading amounts of 5.0 wt% was obtained. For comparison, α-MoC/NHPCs with different loading amounts of α-MoC (α-MoC: 1.4, 2.4, 5.0, 6.8 and 8.1 wt%) while with a similar NP size (~ 3 nm) were fabricated by changing the dosage of Mo12 (20, 40, 60, 80 and 100 mg, respectively). Moreover, NHPC was prepared without the utilization of Mo12.

Characterizations:

X-ray diffraction (XRD) patterns were collected on a PW1820 powder diffractometer (Phillips) using Cu Kα radiation (λ=0.15404 nm) and a scan rate of 0.02 deg. s^{-1}. Infrared spectra were recorded on a FT-IR spectrometer Tensor II (Bruker) with an ATR unit. Raman spectra were recorded with a Bruker RFS 100/S spectrometer at a wavelength of 532 nm. Scanning electron microscopy (SEM), as well as corresponding elemental mapping based on energy-dispersive X-ray spectroscopy (EDX) analysis were carried out with a Gemini 500 (Carl Zeiss) system. Transmission electron microscopy (TEM) and High-resolution TEM (HRTEM) were performed using a LIBRA 200 MC Cs STEM (Carl Zeiss) tool operating at an acceleration voltage of 200 kV. X-ray photoelectron spectroscopy (XPS) experiments were carried out on an AXIS Ultra DLD (Kratos) system using Al Kα radiation, the C1s value was set at 284.6 eV for charge corrections.

Electrochemical measurements:

Prior to the surface coating, glassy carbon rotating disk electrode (RDE, 5 mm in diameter) was polished carefully with 1.0, 0.3 and 0.05 μm alumina powder, respectively, and rinsed with deionized water, followed by sonicated in ethanol and doubly distilled water successively. All catalysts were prepared by mixing 10 mg of the catalysts in 1 mL of solution containing 480 μL of ethanol, 480 μL of H_2O and 40 μL of 5% Nafion solution, followed by ultrasonication for 30 min to form homogeneous catalysts inks. The obtained catalysts inks were then dropped on the surface of pretreated RDE surface and dried before the electrocatalytic tests, leading to 0.2 and 0.1 mg cm^{-2} loading for the obtained samples and Pt/C, respectively. All the electrochemical measurements were carried out on WaveDriver 20 (Pine Research Instrumentation) and CHI 660E Potentiostat systems equipped with a three-electrode cell. All the measurements were performed at ambient temperature in a 0.1 M KOH alkaline solution. A glassy carbon electrode (GCE) coated with the catalyst ink was served as the working electrode, a Ag/AgCl and Pt wire was used as reference and counter electrode, respectively. Potentials in this work were all referred to the reversible hydrogen electrode (RHE) through the Nernst equation as follows: E (*vs.* RHE) = E (*vs*. Ag/AgCl) + 0.197 + 0.05916 × pH. Prior to the measurement, a N_2/O_2 flow was used through the electrolyte in the cell for 30 min to saturate it with N_2/O_2. The electrochemical experiments were conducted in O_2-saturated 0.1 M KOH for the oxygen reduction reaction at room temperature. The RDE tests were measured at various rotating speed from 900 to 2500 rpm with a sweep rate of 10 mV s^{-1}. For the ORR at a RDE, the electron transfer number (*n*) and kinetic current density (J_k) were calculated from the Koutecky-Levich (K-L) equation:

$$\frac{1}{J} = \frac{1}{J_L} + \frac{1}{J_K} = \frac{1}{B\omega^{\frac{1}{2}}} + \frac{1}{J_K}$$

$$B = 0.62nFC_0D_0^{\frac{2}{3}}V^{-\frac{1}{6}}$$

Where *J* is the measured current density, J_K and J_L are the kinetic and limiting current densities, ω is the angular velocity of the disk, n is the electron transfer number, *F* is the Faraday constant (96485 C mol^{-1}), C_0 is the bulk concentration of O_2 (1.2×10^{-6} mol cm^{-3}), D_0 is the diffusion coefficient of O_2 (1.9×10^{-5} cm^2 s^{-1}), and *V* is the kinematic viscosity of the electrolyte (0.01 cm^2 s^{-1}).

The hydrogen peroxide yield (H_2O_2 %) and electron transfer number (n) during the ORR can be determined by a rotating ring-disk electrode (RRDE) technique and calculated *via* the following equations:

$$H_2O_2(\%) = 200 \times \frac{\frac{I_r}{N}}{I_d + \frac{I_r}{N}}$$

$$n = 4 \times \frac{I_d}{I_d + \frac{I_r}{N}}$$

Where I_d is the disk current, I_r is the ring current, and N = 0.37 is the current collection efficiency of the Pt ring.

The accelerated durability tests of the electrocatalysts were performed in the O_2-saturated 0.1 M KOH electrolyte at room temperature by applying potential cycling between 1.0 and 0.6 V *vs*. RHE at a sweep rate of 50 mV s^{-1} for 10000 cycles.

Electrochemical measurements for Zn-air battery:

The primary Zn-air batteries were tested in a home-built electrochemical cell. The homogeneous catalyst ink was loaded on carbon fiber paper with a loading density of 1 mg cm^{-2}, as the air cathode, and a polished Zn foil was used as the anode. A 0.2 M $Zn(OAc)_2$ in 6.0 M KOH aqueous solution was used as the electrolyte.

Computational method and details:

All the DFT simulations were conducted with the Vienna Ab Initio Simulation Package (VASP).[1, 2] The projector augmented wave (PAW) method[3, 4] was applied to describe the electron ion interaction, while the electron exchange and correlation energy was treated within the generalized gradient approximation in the Perdew-Burke-Ernzerhof formalism (GGA-PBE).[5] An energy cut-off of 400 eV was used to get accurate energies with errors less than 1 meV per atom. DFT-D3 method of Grimme was applied to describe the dispersion.[6] The convergence criteria for structure optimization was <0.02 eV/Å for the force and < 10^{-5} eV for energy, respectively. The NC catalyst was modeled by a p(4×4) supercell of graphene doped with nitrogen and the carbon atoms next to pyridinic N were widely accepted to be the active site for ORR,[7] which were constructed as shown in Fig. S20a. The face-centered-cubic δ-MoC phase

has the Fm3m space group and the calculated lattice parameters are a = b = c = 4.376 Å, which is similar with the experimental values of a = b = c = 4.27 Å.[8] A p(3×3) α-MoC(111) surface was used to simulate the ORR reaction mechanism on MoC catalyst as shown in Fig. S20b. Finally, the newly developed MoC/NC material was simulated with a p(3×3) α-MoC(111) surface covered with a layer of NC with pyridinic N as well as defects in the MoC/NC interface, which was shown in Fig. S20c.

In this work, we simulated the four-electron associative oxygen reduction mechanism on three different materials, which involved three different intermediates, that is, *OOH, O*, and OH*. The overall ORR reaction pathway in an alkaline electrolyte could be described as: O_2 (g) + $2H_2O$ (l) + 4e− → $4OH^-$, which involves 1) O_2 (g) + * → O_2*; 2) O_2* + H_2O (l) + e^- → OOH* + OH^-; 3) OOH* + e− → O* + OH^-; 4) O* + H_2O (l) + e^- → OH* + OH^- and 5) OH* + e^- → OH^- + *, where asterisk * denotes the active site. The most stable adsorption configurations of those important intermediates were shown in Fig. S22-S24. The Gibbs free energies of the ORR reaction were simulated with computational hydrogen electrode (CHE) model as developed by Norskov group,[9, 10] which provides an elegant way to describe electrocatalysis reaction mechanisms. In this method, the changes in Gibbs reaction free energy (ΔG_0) for each elementary step is defined as the difference between free energies of the initial and final states, i.e., $\Delta G_0 = \Delta E + \Delta ZPE + \Delta H - T\Delta S$, where $\Delta E = E$(final) - E(initial) is from DFT calculated electronic energies for the initial and final states; ΔZPE, ΔH and ΔS are the differences in zero-point energy, enthalpy and entropy which were calculated within the harmonic approximation for surface species and ideal gas approximation for the gaseous species. The pH effect was incorporated by $\Delta G_{pH} = -kT\ln[H^+] = kT\ln10 \times pH$. The chemical potential of the proton-electron pair was a function of the applied potential ($\Delta G_U = -eU$, where U is the applied electrode potential relative to the standard hydrogen electrode). Eventually, the free energy change for a given elementary step is calculated with $\Delta G = \Delta G_0 + \Delta G_{pH} + \Delta G_U$.

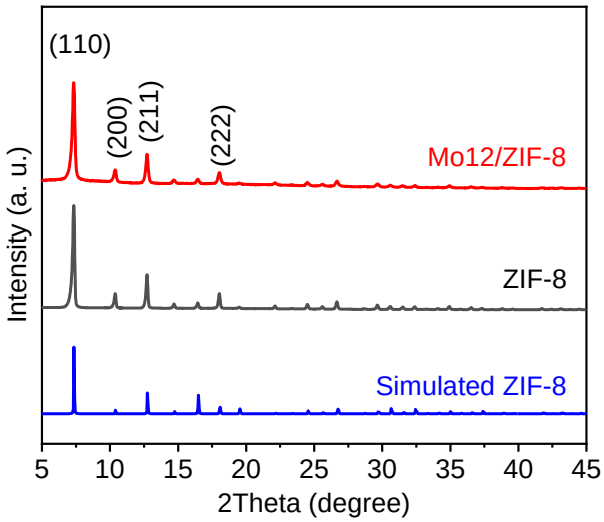

Fig. S1. XRD patterns of ZIF-8 and Mo12/ZIF-8.

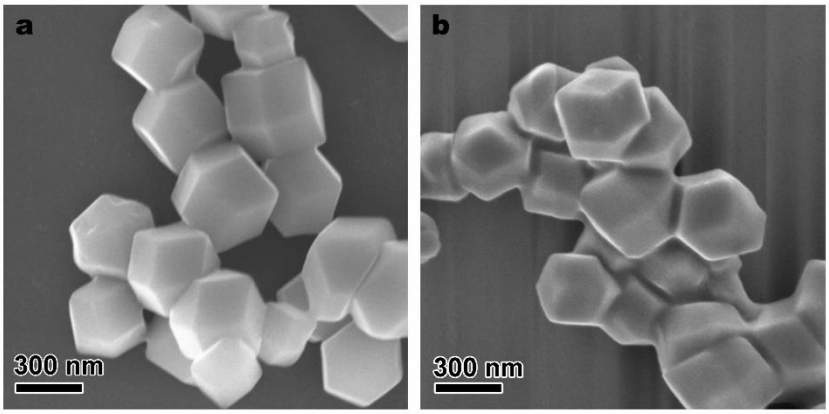

Fig. S2. SEM images of (a) ZIF-8 and (b) Mo12/ZIF-8.

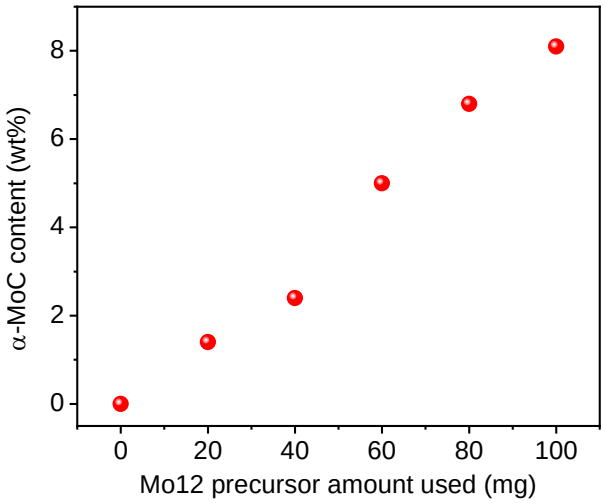

Fig. S3. Synthesis of α-MoC/NHPC with different α-MoC contents by changing the dosage of Mo12.

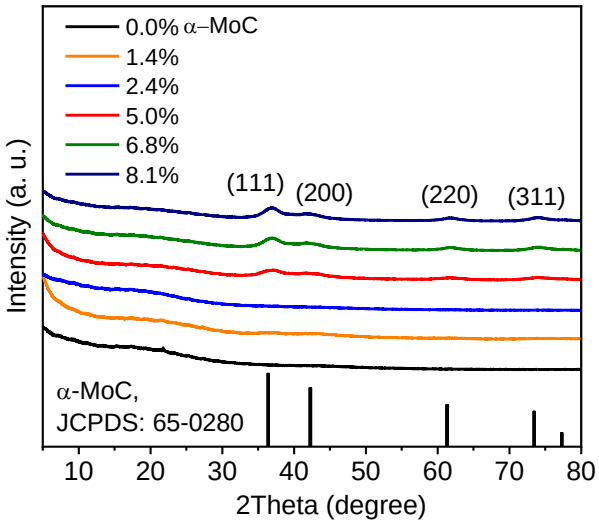

Fig. S4. XRD patterns of α-MoC/NHPCs with different α-MoC contents.

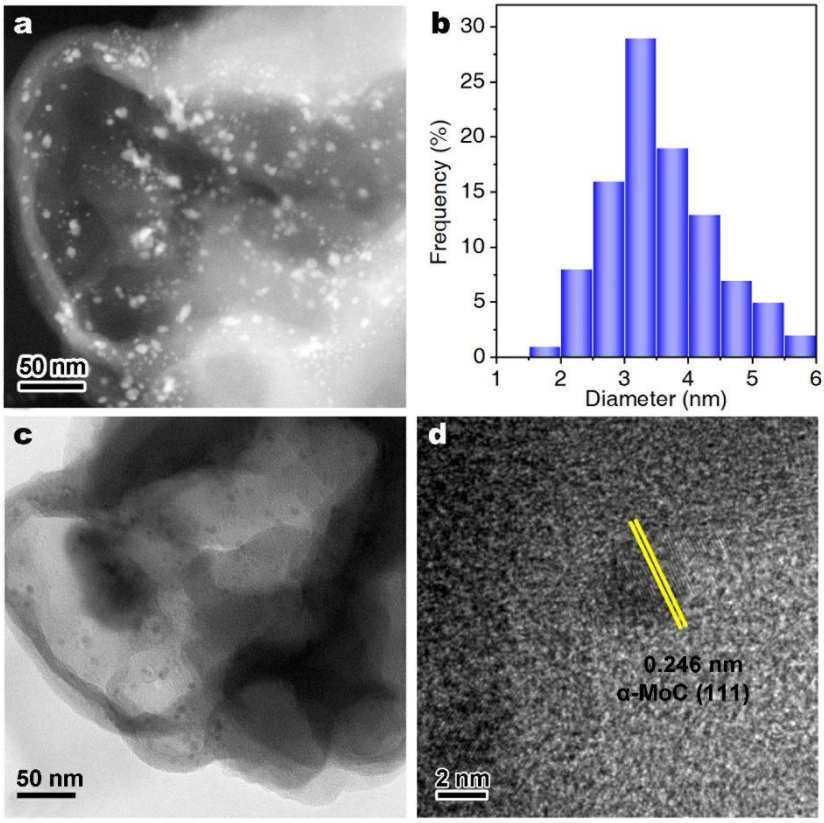

Fig. S5. (a) HAADF–STEM, (b) the corresponding α-MoC NP size distribution, (c) TEM and (d) HRTEM images of α-MoC/NHPC with a α-MoC content of 1.4 wt%.

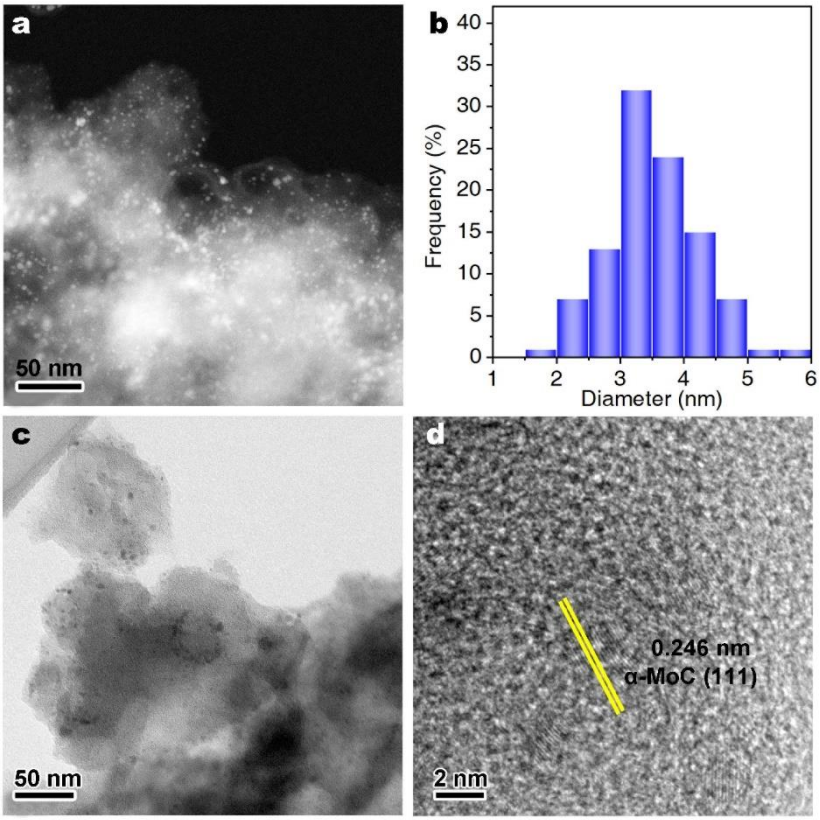

Fig. S6. (a) HAADF–STEM, (b) the corresponding α-MoC NP size distribution, (c) TEM and (d) HRTEM images of α-MoC/NHPC with a α-MoC content of 2.4 wt%.

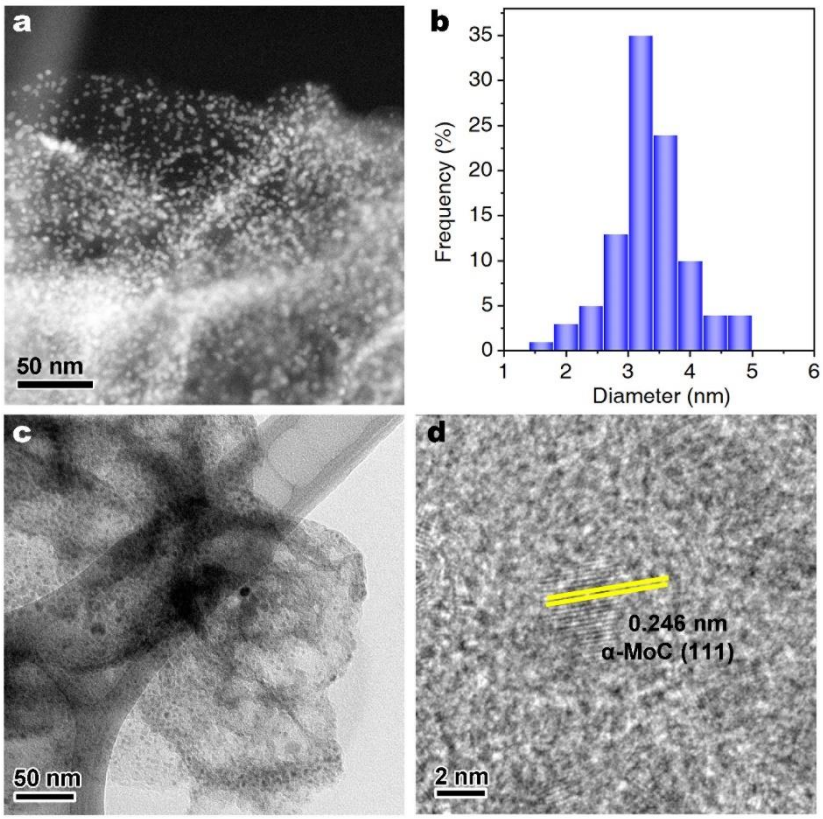

Fig. S7. (a) HAADF–STEM, (b) the corresponding α-MoC NP size distribution, (c) TEM and (d) HRTEM images of α-MoC/NHPC with a α-MoC content of 6.8 wt%.

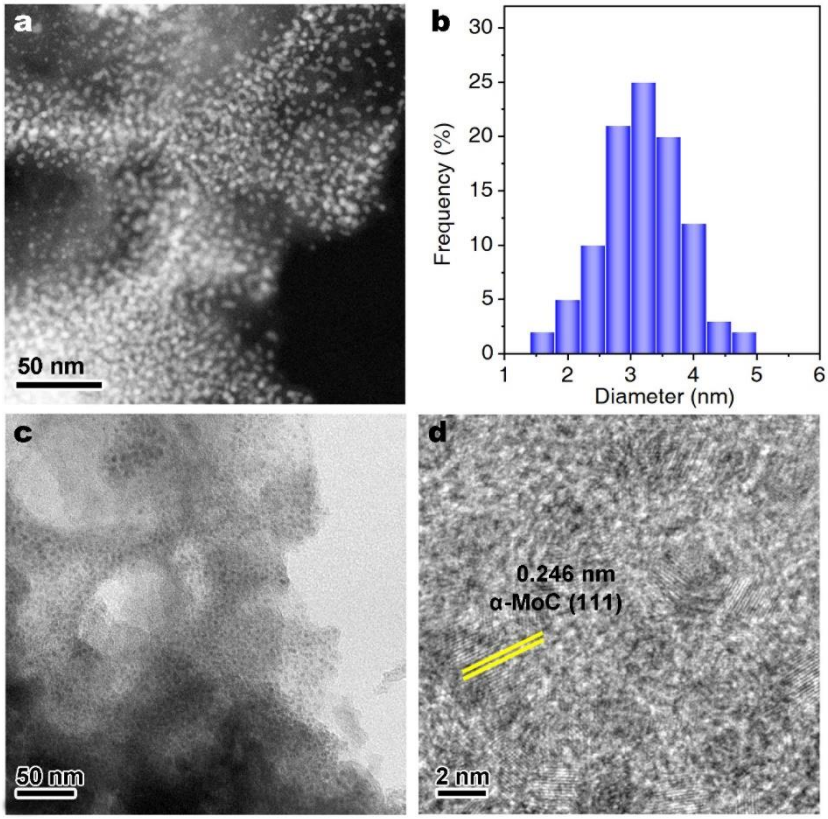

Fig. S8. (a) HAADF–STEM, (b) the corresponding α-MoC NP size distribution, (c) TEM and (d) HRTEM images of α-MoC/NHPC with a α-MoC content of 8.1 wt%.

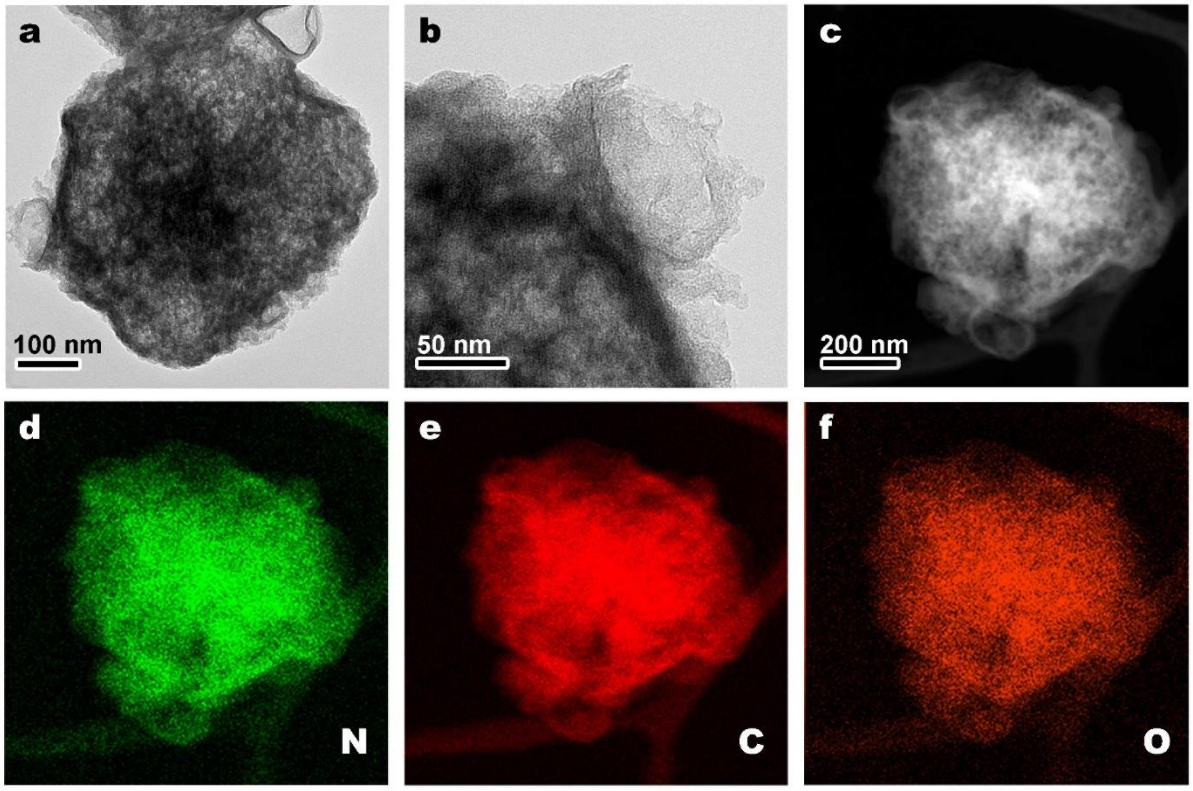

Fig. S9. (a, b) TEM, (c) HAADF-STEM images of NHPC and corresponding EDX elemental mapping images of (d) N, (e) C and (f) O elements in NHPC.

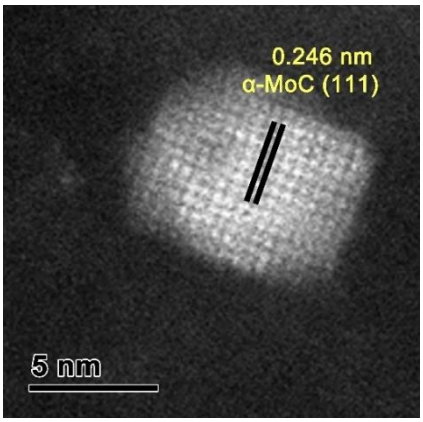

Fig. S10. High-resolution STEM image of α-MoC/NHPC.

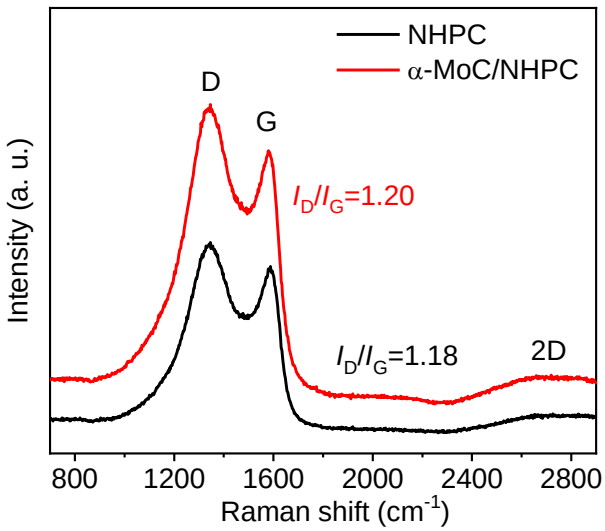

Fig. S11. Raman spectra of NHPC and α-MoC/NHPC.

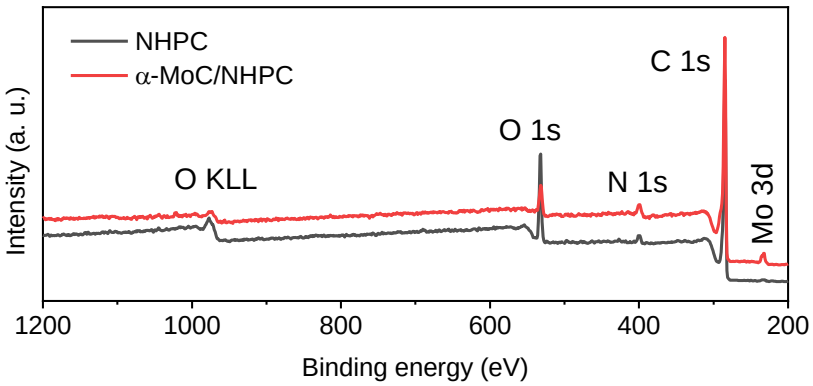

Fig. S12. XPS survey spectra of NHPC and α-MoC/NHPC.

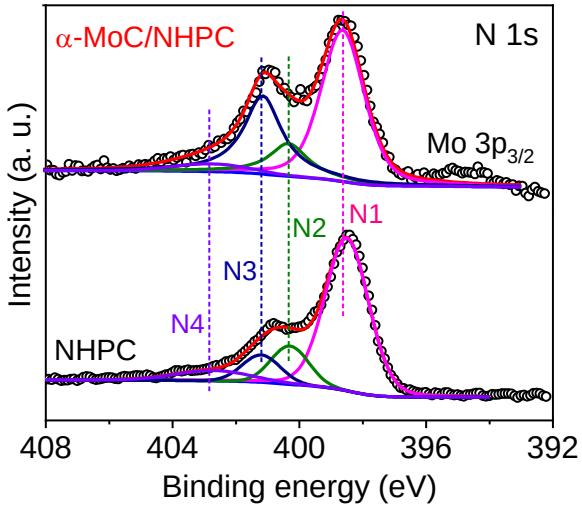

Fig. S13. High-resolution N 1s XPS spectra (N1: pyridinic N, N2: pyrrolic N, N3: graphitic N, N4: oxidized N) of NHPC and α-MoC/NHPC. The broad peak at binding energies of 396-393 eV for α-MoC/NHPC was contributed to Mo $3p_{2/3}$.[11]

Table S1. Elemental composition (at%) of NHPC and α-MoC/NHPC.

Catalyst	C (%)	O (%)	N (%)	N species			
				pyridinic N (%)	pyrrolic N (%)	graphitic N (%)	oxidized N (%)
NHPC	79.6	12.4	8.0	5.5	1.1	0.8	0.6
α-MoC/NHPC	81.6	9.0	6.7	4.8	0.9	0.7	0.3

The C, O and N contents were determined by elemental analysis. The proportions of four types of N species were calculated by the fitting of high-resolution N 1s XPS spectra of NHPC and α-MoC/NHPC (Fig. S13).

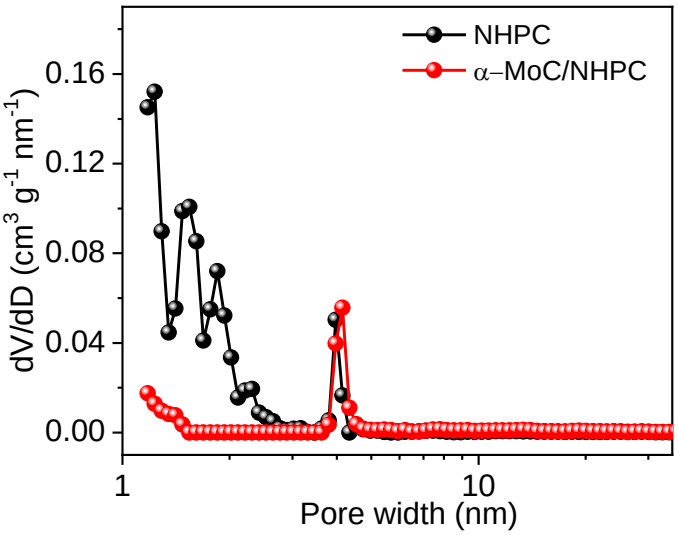

Fig. S14. Pore size distribution curves of NHPC and α-MoC/NHPC.

Table S2. Summary of reported ORR performance of earth-abundant electrocatalysts. All catalysts were evaluated in 0.1 M KOH aqueous solution.

Catalyst	$E_{1/2}$ (V *vs*. RHE)	J_k (mA cm^{-2}) at 0.8 V	Reference
α-MoC/NHPC	**0.88**	**33.8**	**This work**
NHPC	0.84	17.8	This work
Pt/C	0.85	21.4	This work
NCNTFs	0.87	~4.0	*Nat. Energy* 2016, **1**, 15006.[12]
CoZIF-VXC72	0.84	-	*Adv. Mater.* 2017, **29**, 1701354.[13]
h-Mn_3O_4-MSLs	0.84	<1.0	*J. Am. Chem. Soc.* 2017, **139**, 12133.[14]
CoO_x NPs/BNG	0.81	-	*Angew. Chem., Int. Ed.* 2017, **56**, 7121.[15]
$Mo_{0.42}C_{0.58}$@N−C	0.828	-	*ChemistrySelect* 2018, **3**, 5106.[16]
Mo_2C@NC	0.872	~13.0	*Adv. Funct. Mater*. 2018, **28**, 1705967.[17]
C/α-MoC/Ag	~0.80	-	*J. Phys. Chem. Lett*. 2018, **9**, 779.[18]
Co-ISAS/p-CN	0.838	5.2 @ 0.83 V	*Adv. Mater*. 2018, **30**, 1706508.[19]
Cu-N-C	0.869	11.8 @ 0.85 V	*Energy Environ. Sci*. 2018, **11**, 2263.[20]
Fe2-Z8-C	0.871	-	*Angew. Chem., Int. Ed.* 2018, **57**, 1204.[21]
ZnCoNC-0.1	0.84	~1.8 @ 0.85 V	*Nano Res*. 2018, **11**, 163.[22]
NLPC	~0.83	-	*Adv. Funct. Mater.* 2018, **28**, 1705356.[23]
HLCT	0.88	4.4 @ 0.85 V	*Adv. Funct. Mater.* 2019, **29**, 1900015.[24]
$Mn_{1.5}Co_{1.5}O_4$	0.822	-	*Appl. Catal. B: Environ.* 2019, **244**, 536.[25]
Fe-NC SAC	0.90	-	*Nat. Commun.* 2019, **10**, 1278.[26]
PcCu-O_8 -Co/CNT	0.83	<10.0	*Angew. Chem. Int. Ed.* 2019, **58**, 10677.[27]
FeNPC	0.88	-	*J. Mater. Chem. A*, 2019, **7**, 14732.[28]
$N_{0.54}$–Z_3/M_1-900	0.825	<1.0	*Energy Environ. Sci.*, 2019, **12**, 648.[29]
Fe-SAs/NSC	0.87	35.9	*J. Am. Chem. Soc*. 2019, **141**, 20118.[30]
porous carbon-Fe	0.869	-	*Angew. Chem., Int. Ed.* 2019, **58**, 4963.[31]
LTHT-FeP aerogel	0.83	-	*Angew. Chem., Int. Ed.* 2020, **59**, 2483.[32]
Mo SACs/N-C	0.83	~4.0	*Nano Energy* 2020, **67**, 104288.[33]
Fe/OES	0.85	-	*Angew. Chem., Int. Ed*. 2020, **59**, 7384.[34]

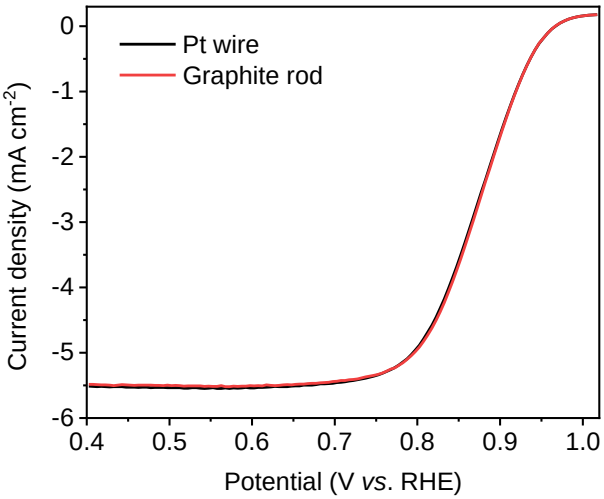

Fig. S15. LSV polarization curves of the α-MoC/NHPC in O_2-saturated 0.1 M KOH solution using Pt wire and graphite rod as counter electrodes.

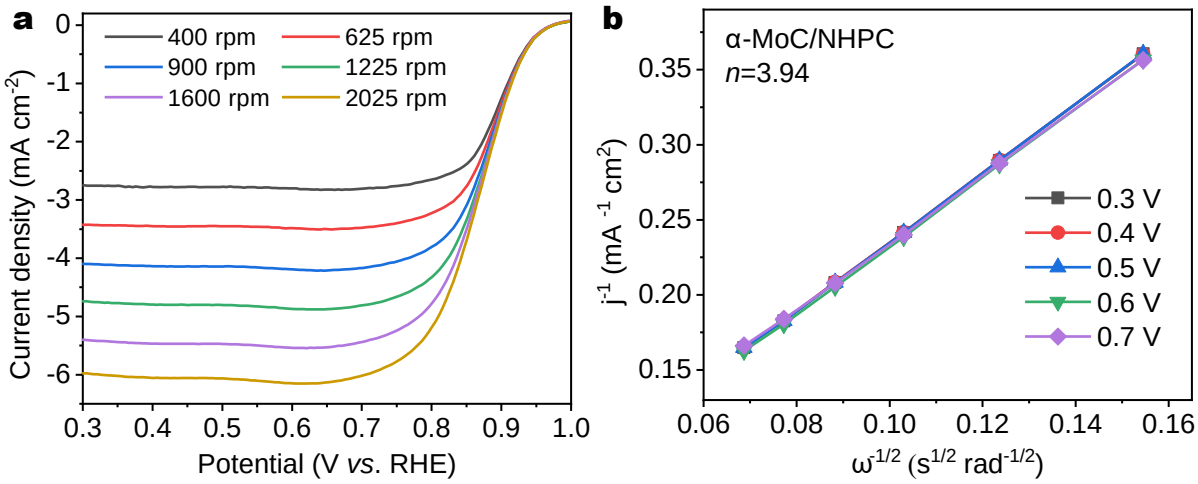

Fig. S16. (a) LSV polarization curves of the α-MoC/NHPC in O_2-saturated 0.1 M KOH at a sweep rate of 5 mVs^{-1} with different rotation rates (400~2025 rpm) and (b) the corresponding K-L plots (j^{-1} *versus* $\omega^{-1/2}$) at different potentials.

To probe ORR kinetics, rotating disk electrode (RDE) measurement at different rotation speeds were operated (Fig. 16a) and the related Koutecký–Levich (K-L) plots were acquired. Fig. S16b shows the linear and almost parallel K-L plots at different applied potentials, reflecting a first-order reaction kinetics toward the concentration of dissolved oxygen and a similar electron transfer number (n) at α-MoC/NHPC electrode. The electron transfer number (n) of α-MoC/NHPC was calculated to be 3.94 at 0.40 V, indicating a four-electron oxygen reduction process.

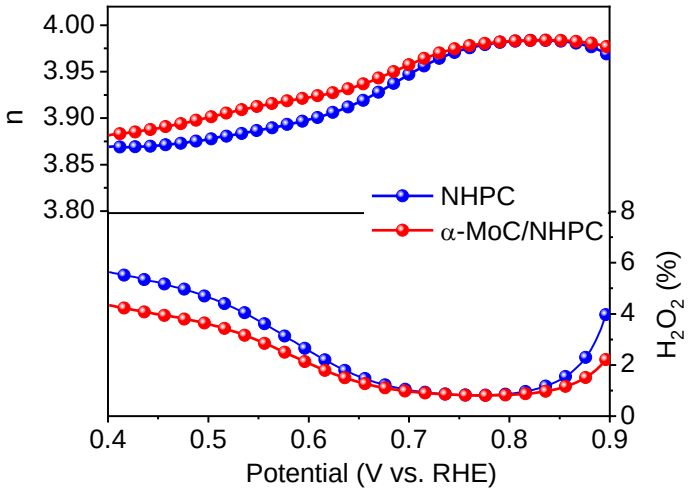

Fig. S17. Electron transfer numbers and H_2O_2 yield plots of NHPC and α-MoC/NHPC.

To quantify the ORR pathway, a rotating ring-disk electrode (RRDE) technique was carried out to monitor the generation of H_2O_2 during the ORR process. The H_2O_2 yield of α-MoC/NHPC was below 4.5% at the potential range from 0.40 to 0.90 V, revealing a superior ORR selectivity toward OH^- formation (Fig. S17).

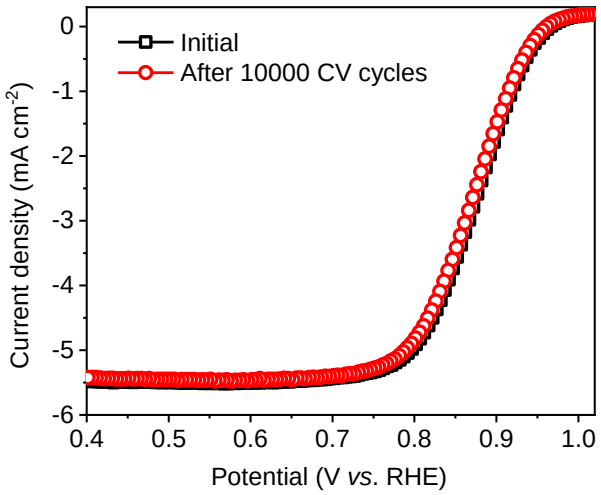

Fig. S18. ORR polarization curves of α-MoC/NHPC before and after 10000 CV cycles using a graphite rod as counter electrode.

The electrocatalytic durability is another important criterion for accessing the ORR performance of a catalyst. As shown in Fig. S18, after 10000 cyclic voltammetry (CV) scans between 0.6 and 1.0 V at a scan rate of 50 mV s^{-1} in 0.1 M KOH aqueous solution under O_2 atmosphere, the $E_{1/2}$ of the α-MoC/NHPC decreased by only 2 mV, unambiguously suggesting a superior ORR stability.

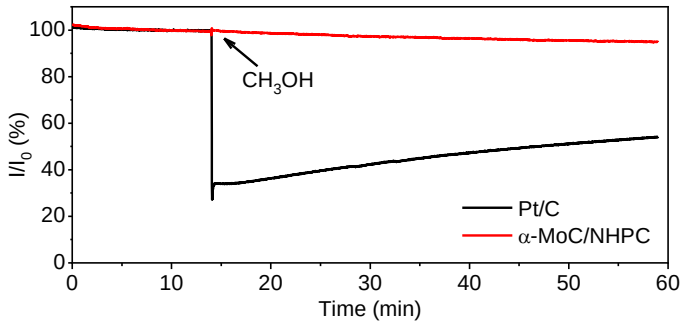

Fig. S19. *I*–*t* CA responses for α-MoC/NHPC and Pt/C at 0.4 V and 1600 rpm with 2% (*v*/*v*) methanol addition at around 800 s. I_0 defines the initial current.

Methanol tolerances of the α-MoC/NHPC and Pt/C were assessed using *i*-*t* chronoamperometry (CA) tests. As revealed in Fig. S19, in comparison with sharply decreased current density of Pt/C after injecting 2% *(v/v)* methanol, the current density of α-MoC/NHPC showed negligible decrease.

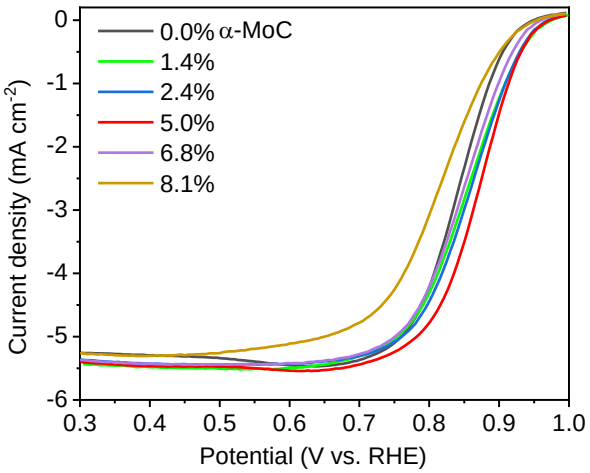

Fig. S20. ORR polarization curves of α-MoC/NHPCs with different α-MoC contents.

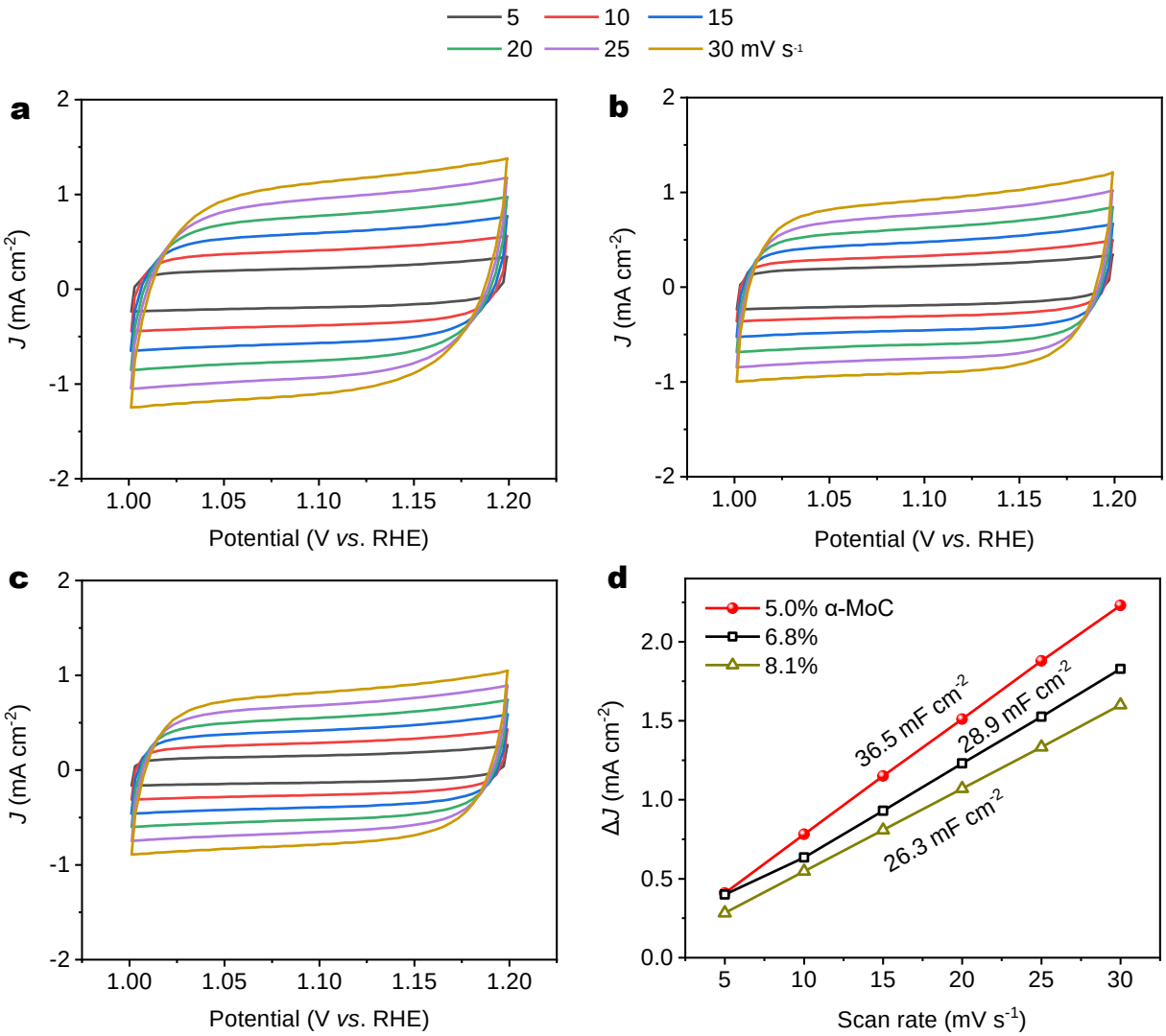

Fig. 21. Cyclic voltammetry curves collected at different scan rates for α-MoC/NHPCs with different α-MoC contents: (a) 5.0 wt%, (b) 6.8 wt% and (c) 8.1 wt%. (d) Charge current density differences (Δ*J*) at 1.10 V (*vs*. RHE) for α-MoC/NHPCs plotted against scan rate.

The electrochemically active surface areas (ECSA) were studied based on the electrochemical double-layer capacitance of the electrocatalysts at non-faradaic overpotentials. By plotting the difference of current density (*J*) between the anodic and cathodic sweeps ($J_{anodic} - J_{cathodic}$) at 1.10 V *vs*. RHE against the scan rate (ν), a linear trend was observed. The slope of the fitting line is equal to twice the geometric double layer capacitance (C_{dl}), which is proportional to the effective electrode surface area of the materials. As disclosed in Fig. 21, the C_{dl} of α-MoC/NHPC (6.8 wt%) was calculated to be 28.9 mF cm^{-2}, which was smaller than 36.5 mF cm^{-2} for α-MoC/NHPC (5.0 wt%). This result indicated a smaller ECSA of α-MoC/NHPC (6.8 wt%) than that of α-MoC/NHPC (5.0 wt%).

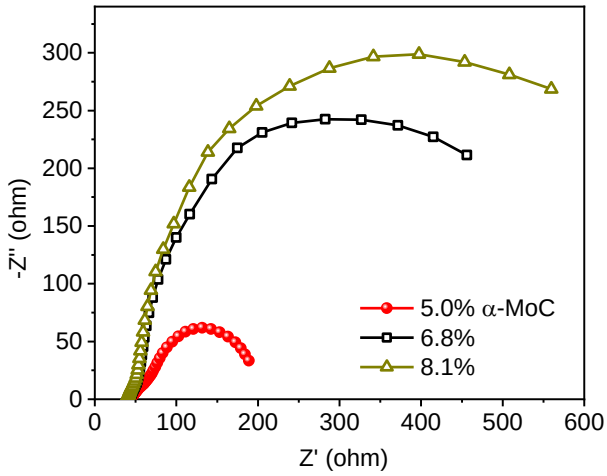

Fig. S22. Electrochemical impedance spectroscopy (EIS) analyses of α-MoC/NHPCs with different α-MoC content.

Electrochemical impedance spectroscopy (EIS) was recorded in O_2-saturated 0.1 M KOH at 0.85 V *vs*. RHE with an alternating current voltage amplitude of 10 mV from 10 kHz to 0.01 Hz and an electrode rotation speed of 1600 rpm. As revealed in Fig. S22, the α-MoC/NHPC (6.8 wt%) demonstrated a slower ORR kinetics than that of α-MoC/NHPC (5.0 wt%).

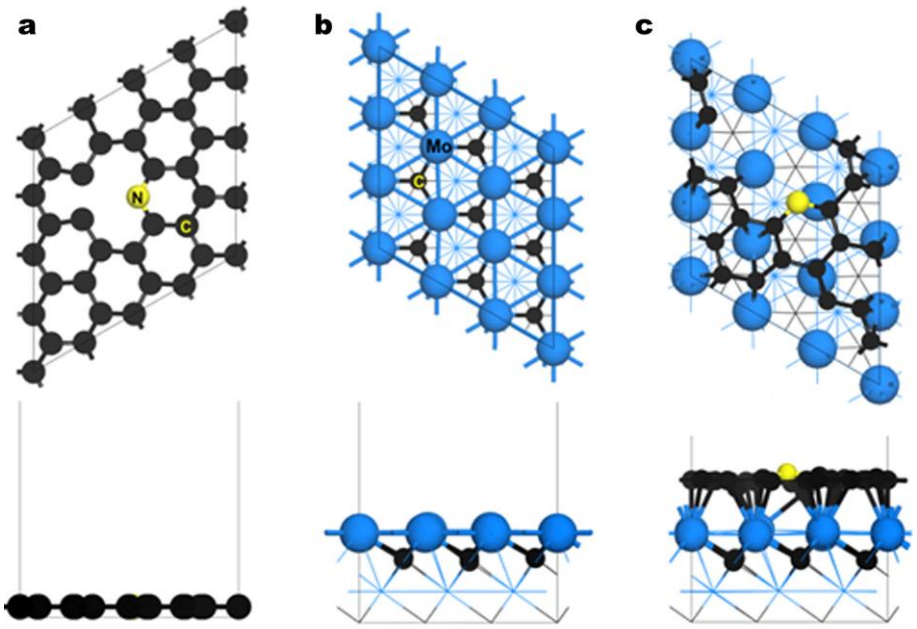

Fig. S23. Structures of (a) NC, (b) α-MoC (111) and (c) α-MoC/NC surfaces.

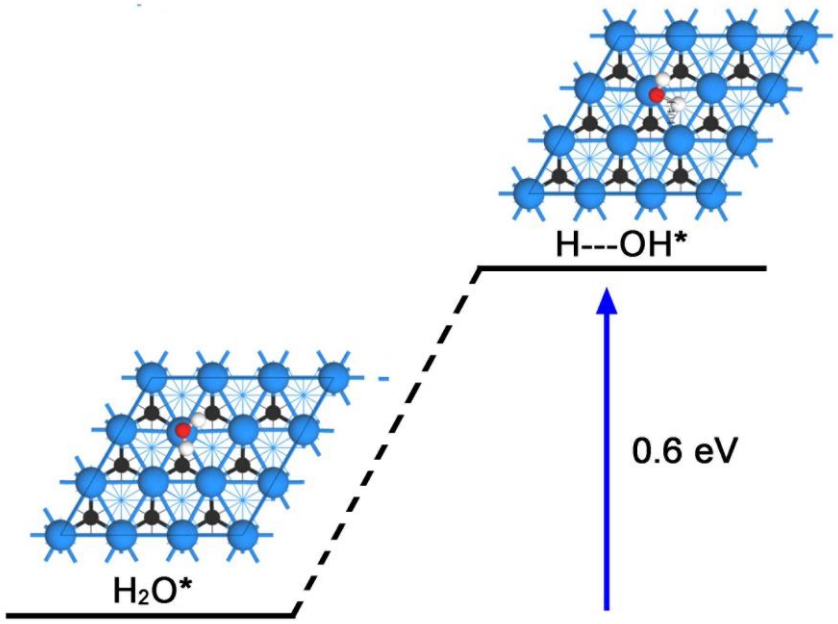

Fig. S24. Schematic energy diagram for water dissociation and corresponding initial/transition states of water adsorption configurations on α-MoC (111) surface.

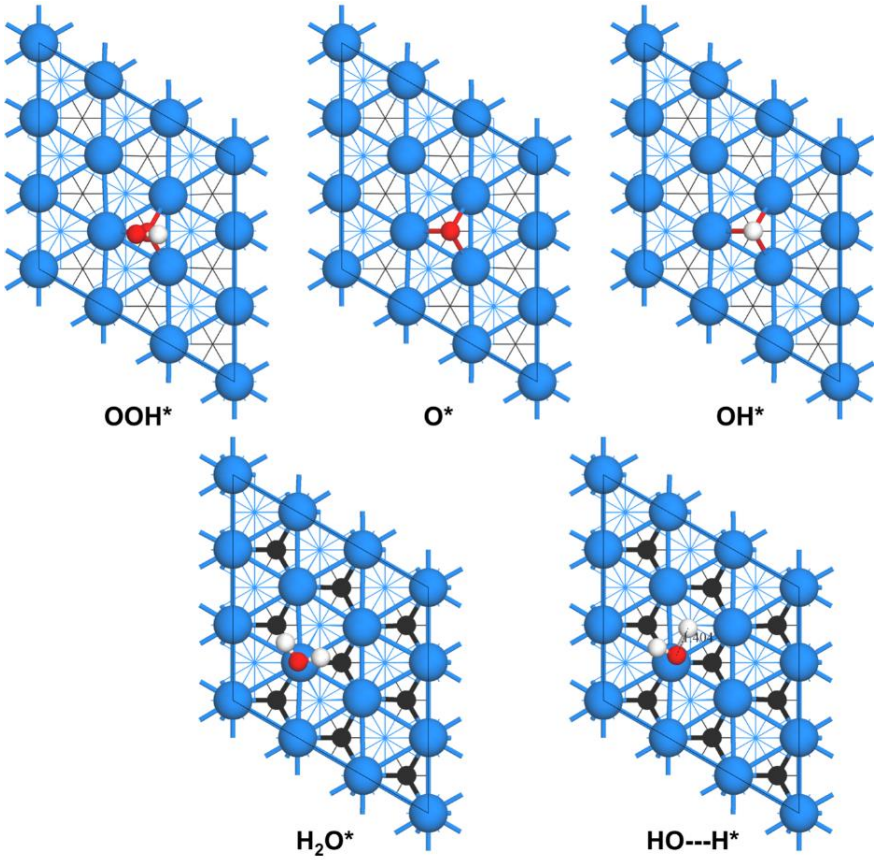

Fig. S25. Adsorption configurations of OOH, O, OH and H_2O as well as transition state structure of H_2O dissociation (HO---H*) on α-MoC surface.

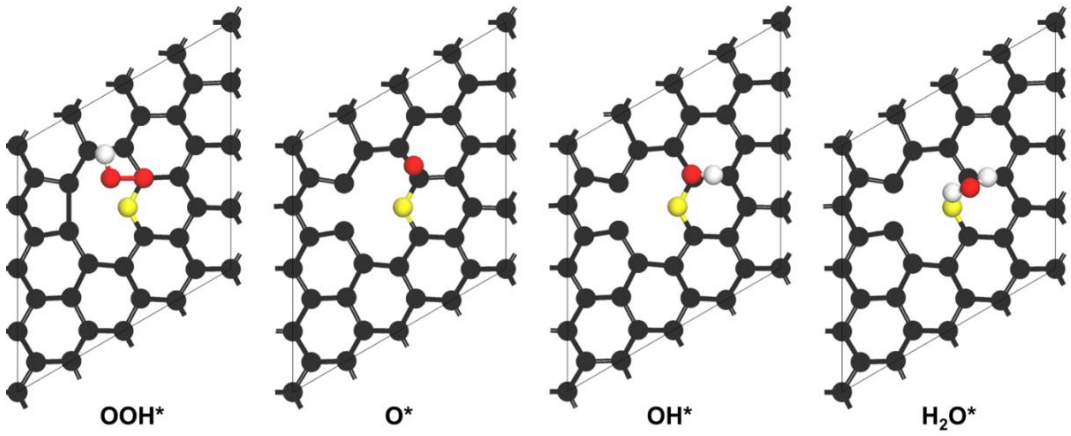

Fig. S26. Adsorption configurations of OOH, O, OH and H_2O on NC surface.

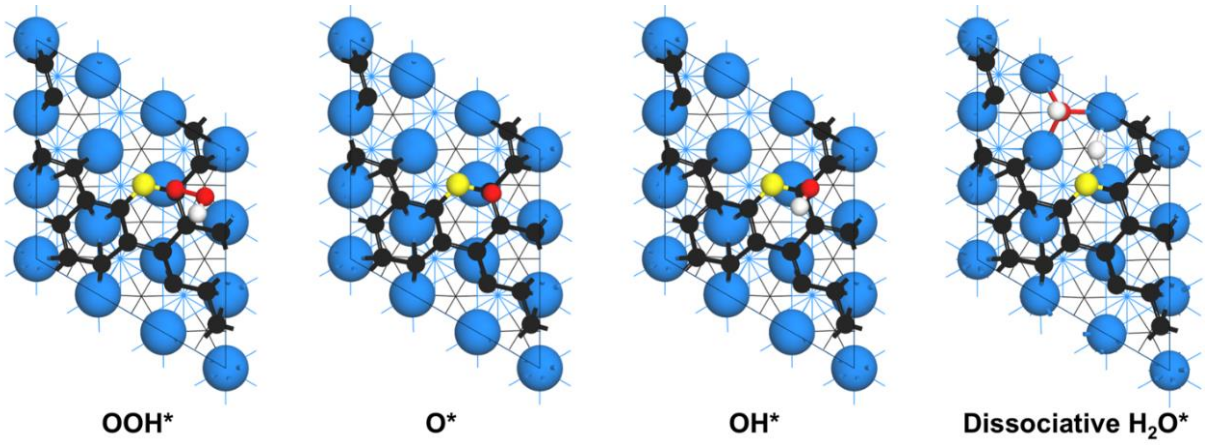

Fig. S27. Adsorption configurations of OOH, O and OH as well as dissociative H_2O adsorption on α-MoC/NC surface.

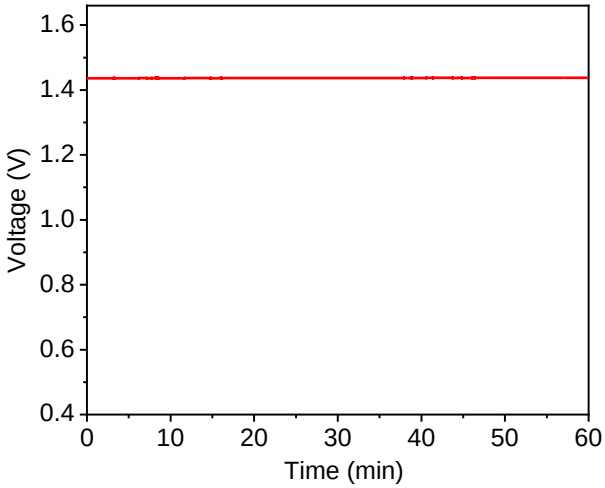

Fig. S28. Open circuit voltage measurement of a Zn-Air battery with α-MoC/NHPC as the cathode catalyst.

Table S3. The performance of Zn-air batteries with various reported electrocatalysts.

Catalyst	Peak power density (mW cm^{-2})	Durability (h)	Reference
α-MoC/NHPC	**200.3**	**240**	**This work**
20% Pt/C	154.1	-	This work
NPMC-1000	55	240	*Nat. Nanotechnol.* 2015, 10, 444.[35]
N-GRW	65	30	*Sci. Adv.* 2016, **2**, 1501122.[36]
Co-N_x-C	152	>60	*Adv. Mater.* 2017, **29**, 1703185.[37]
S-GNS/$NiCo_2S_4$	216.3	100	*Adv. Funct. Mater.* 2018, **28**, 1706675.[38]
N/E-HPC-900	192.7	110	*Adv. Mater.* 2019, **31**, 1900341.[39]
CoNi-SAs/NC	101.4	>30	*Adv. Mater.* 2019, **31**, 1905622.[40]
MnO/Co/PGC	172	>100	*Adv. Mater.* 2019, **31**, 1902339.[41]
Co/Co–N–C	132	~330	*Adv. Mater*. 2019, **31**, 1901666.[42]
PdMo bimetallene	154.2	>115	*Nature* 2019, **574**, 81.[43]
Co_2FeO_4/NCNTs	90.7	100	*Angew. Chem. Int. Ed*. 2019, **58**, 13291.[44]
Co_3O_{4-x} HoNPs@HPNCS	94.1	>16	*Angew. Chem. Int. Ed.* 2019, **58**, 13840.[45]
N‑$CoSe_2$/3D-MXene	142	166	*ACS Materials Lett*. 2019, **1**, 432.
3DOM-Co@TiO_xN_y	110	300	*Adv. Mater.* 2019, **31**, 1806761.[46]
Bi–CoP/NP-DG	112	58	*J. Mater. Chem. A*, 2019, **7**, 22507.[47]
Mo SACs/N-C	112	120	*Nano Energy* 2020, **67**, 104288.[33]
CoS_x@Cu_2MoS_4-MoS_2/NSG	40	-	*Adv. Energy Mater*. 2020, **10**, 1903289.[48]
Fe_2Ni@NC	126	500	*Adv. Energy Mater.* 2020, **10**, 1903003.[49]
W_2N/WC	172	18	*Adv. Mater.* 2020, **32**, 1905679.[50]
Pt-SCFP/C-12	112	80	*Adv. Energy Mater*. 2020, **10**, 1903271.[51]
$FeNi_3$@NC	139	30	*Appl. Catal. B: Environ.* 2020, **268**, 118729.[52]
SA-PtCoF	125	240	*Energy Environ. Sci.* 2020, **13**, 884.[53]

References

1. G. Kresse and J. Furthmüller, *Comput. Mater. Sci.*, 1996, **6**, 15-50.
2. G. Kresse and J. Furthmüller, *Phys. Rev. B*, 1996, **54**, 11169-11186.
3. P. E. Blöchl, *Phys. Rev. B*, 1994, **50**, 17953-17979.
4. G. Kresse and D. Joubert, *Phys. Rev. B*, 1999, **59**, 1758-1775.
5. J. P. Perdew, K. Burke and M. Ernzerhof, *Phys. Rev. Lett.*, 1996, **77**, 3865-3868.
6. S. Grimme, J. Antony, S. Ehrlich and H. Krieg, *J. Chem. Phys.*, 2010, **132**, 154104.
7. D. Guo, R. Shibuya, C. Akiba, S. Saji, T. Kondo and J. Nakamura, *Science*, 2016, **351**, 361-365.
8. E. Clougherty, K. Lothrop and J. Kafalas, *Nature*, 1961, **191**, 1194-1194.
9. J. K. Nørskov, J. Rossmeisl, A. Logadottir, L. Lindqvist, J. R. Kitchin, T. Bligaard and H. Jónsson, *J. Phys. Chem. B*, 2004, **108**, 17886-17892.
10. A. A. Peterson, F. Abild-Pedersen, F. Studt, J. Rossmeisl and J. K. Nørskov, *Energy Environ. Sci.*, 2010, **3**, 1311-1315.
11. J.-S. Li, Y. Wang, C.-H. Liu, S.-L. Li, Y.-G. Wang, L.-Z. Dong, Z.-H. Dai, Y.-F. Li and Y.-Q. Lan, *Nat. Commun.*, 2016, **7**, 11204.
12. B. Y. Xia, Y. Yan, N. Li, H. B. Wu, X. W. Lou and X. Wang, *Nat. Energy*, 2016, **1**, 15006.
13. B. Ni, C. Ouyang, X. Xu, J. Zhuang and X. Wang, *Adv. Mater.*, 2017, **29**, 1701354.
14. T. Li, B. Xue, B. Wang, G. Guo, D. Han, Y. Yan and A. Dong, *J. Am. Chem. Soc.*, 2017, **139**, 12133-12136.
15. Y. Tong, P. Chen, T. Zhou, K. Xu, W. Chu, C. Wu and Y. Xie, *Angew. Chem., Int. Ed.*, 2017, **56**, 7121-7125.
16. H. Wang, Y. Yu, J. Wei, X. Yu, G. Chen, J. Ma and S. Xing, *ChemistrySelect*, 2018, **3**, 5106-5112.
17. Z. Cheng, Q. Fu, Q. Han, Y. Xiao, Y. Liang, Y. Zhao and L. Qu, *Adv. Funct. Mater.*, 2018, **28**, 1705967.
18. L. Cao, P. Tao, M. Li, F. Lyu, Z. Wang, S. Wu, W. Wang, Y. Huo, L. Huang and Z. Lu, *J. Phys. Chem. Lett.*, 2018, **9**, 779-784.
19. A. Han, W. Chen, S. Zhang, M. Zhang, Y. Han, J. Zhang, S. Ji, L. Zheng, Y. Wang, L. Gu, C. Chen, Q. Peng, D. Wang and Y. Li, *Adv. Mater.*, 2018, **30**, 1706508.
20. F. Li, G.-F. Han, H.-J. Noh, S.-J. Kim, Y. Lu, H. Y. Jeong, Z. Fu and J.-B. Baek, *Energy Environ. Sci.*, 2018, **11**, 2263-2269.

21. Q. Liu, X. Liu, L. Zheng and J. Shui, *Angew. Chem., Int. Ed.*, 2018, **57**, 1204-1208.
22. X. Wu, G. Meng, W. Liu, T. Li, Q. Yang, X. Sun and J. Liu, *Nano Res.*, 2018, **11**, 163-173.
23. Y. Wang, L. Tao, Z. Xiao, R. Chen, Z. Jiang and S. Wang, *Adv. Funct. Mater.*, 2018, **28**, 1705356.
24. Y. Dong, M. Zhou, W. Tu, E. Zhu, Y. Chen, Y. Zhao, S. Liao, Y. Huang, Q. Chen and Y. Li, *Adv. Funct. Mater.*, 2019, **29**, 1900015.
25. K. Li, R. Zhang, R. Gao, G.-Q. Shen, L. Pan, Y. Yao, K. Yu, X. Zhang and J.-J. Zou, *Appl. Catal. B: Environ.*, 2019, **244**, 536-545.
26. L. Zhao, Y. Zhang, L.-B. Huang, X.-Z. Liu, Q.-H. Zhang, C. He, Z.-Y. Wu, L.-J. Zhang, J. Wu, W. Yang, L. Gu, J.-S. Hu and L.-J. Wan, *Nat. Commun.*, 2019, **10**, 1278.
27. H. Zhong, K. H. Ly, M. Wang, Y. Krupskaya, X. Han, J. Zhang, J. Zhang, V. Kataev, B. Büchner, I. M. Weidinger, S. Kaskel, P. Liu, M. Chen, R. Dong and X. Feng, *Angew. Chem., Int. Ed.*, 2019, **58**, 10677-10682.
28. X. Zhu, X. Tan, K.-H. Wu, C.-L. Chiang, Y.-C. Lin, Y.-G. Lin, D.-W. Wang, S. Smith, X. Lu and R. Amal, *J. Mater. Chem. A*, 2019, **7**, 14732-14742.
29. X. Li, B. Y. Guan, S. Gao and X. W. Lou, *Energy Environ. Sci.*, 2019, **12**, 648-655.
30. J. Zhang, Y. Zhao, C. Chen, Y.-C. Huang, C.-L. Dong, C.-J. Chen, R.-S. Liu, C. Wang, K. Yan, Y. Li and G. Wang, *J. Am. Chem. Soc.*, 2019, **141**, 20118-20126.
31. J. Xie, B.-Q. Li, H.-J. Peng, Y.-W. Song, J.-X. Li, Z.-W. Zhang and Q. Zhang, *Angew. Chem., Int. Ed.*, 2019, **58**, 4963-4967.
32. N. Zion, D. A. Cullen, P. Zelenay and L. Elbaz, *Angew. Chem., Int. Ed.*, 2020, **59**, 2483-2489.
33. Z. Kou, W. Zang, Y. Ma, Z. Pan, S. Mu, X. Gao, B. Tang, M. Xiong, X. Zhao, A. K. Cheetham, L. Zheng and J. Wang, *Nano Energy*, 2020, **67**, 104288.
34. C.-C. Hou, L. Zou, L. Sun, K. Zhang, Z. Liu, Y. Li, C. Li, R. Zou, J. Yu and Q. Xu, *Angew. Chem., Int. Ed.*, 2020, **59**, 7384-7389.
35. J. Zhang, Z. Zhao, Z. Xia and L. Dai, *Nat. Nanotechnol.*, 2015, **10**, 444.
36. H. B. Yang, J. Miao, S.-F. Hung, J. Chen, H. B. Tao, X. Wang, L. Zhang, R. Chen, J. Gao, H. M. Chen, L. Dai and B. Liu, *Sci. Adv.*, 2016, **2**, 1501122.
37. C. Tang, B. Wang, H.-F. Wang and Q. Zhang, *Adv. Mater.*, 2017, **29**, 1703185.
38. W. Liu, J. Zhang, Z. Bai, G. Jiang, M. Li, K. Feng, L. Yang, Y. Ding, T. Yu, Z. Chen and A. Yu, *Adv. Funct. Mater.*, 2018, **28**, 1706675.

39. X. Peng, L. Zhang, Z. Chen, L. Zhong, D. Zhao, X. Chi, X. Zhao, L. Li, X. Lu, K. Leng, C. Liu, W. Liu, W. Tang and K. P. Loh, *Adv. Mater.*, 2019, **31**, 1900341.

40. X. Han, X. Ling, D. Yu, D. Xie, L. Li, S. Peng, C. Zhong, N. Zhao, Y. Deng and W. Hu, *Adv. Mater.*, 2019, **0**, 1905622.

41. X. F. Lu, Y. Chen, S. Wang, S. Gao and X. W. Lou, *Adv. Mater.*, 2019, **31**, 1902339.

42. P. Yu, L. Wang, F. Sun, Y. Xie, X. Liu, J. Ma, X. Wang, C. Tian, J. Li and H. Fu, *Adv. Mater.*, 2019, **31**, 1901666.

43. M. Luo, Z. Zhao, Y. Zhang, Y. Sun, Y. Xing, F. Lv, Y. Yang, X. Zhang, S. Hwang, Y. Qin, J.-Y. Ma, F. Lin, D. Su, G. Lu and S. Guo, *Nature*, 2019, **574**, 81-85.

44. X.-T. Wang, T. Ouyang, L. Wang, J.-H. Zhong, T. Ma and Z.-Q. Liu, *Angew. Chem., Int. Ed.*, 2019, **58**, 13291-13296.

45. D. Ji, L. Fan, L. Tao, Y. Sun, M. Li, G. Yang, T. Q. Tran, S. Ramakrishna and S. Guo, *Angew. Chem., Int. Ed.*, 2019, **58**, 13840-13844.

46. G. Liu, J. Li, J. Fu, G. Jiang, G. Lui, D. Luo, Y.-P. Deng, J. Zhang, Z. P. Cano, A. Yu, D. Su, Z. Bai, L. Yang and Z. Chen, *Adv. Mater.*, 2019, **31**, 1806761.

47. J. Chen, B. Ni, J. Hu, Z. Wu and W. Jin, *J. Mater. Chem. A*, 2019, **7**, 22507-22513.

48. D. C. Nguyen, D. T. Tran, T. L. L. Doan, D. H. Kim, N. H. Kim and J. H. Lee, *Adv. Energy Mater.*, 2020, **10**, 1903289.

49. J. Zhu, M. Xiao, G. Li, S. Li, J. Zhang, G. Liu, L. Ma, T. Wu, J. Lu, A. Yu, D. Su, H. Jin, S. Wang and Z. Chen, *Adv. Energy Mater.*, 2020, **10**, 1903003.

50. J. Diao, Y. Qiu, S. Liu, W. Wang, K. Chen, H. Li, W. Yuan, Y. Qu and X. Guo, *Adv. Mater.*, 2020, **32**, 1905679.

51. X. Wang, J. Sunarso, Q. Lu, Z. Zhou, J. Dai, D. Guan, W. Zhou and Z. Shao, *Adv. Energy Mater.*, 2020, **10**, 1903271.

52. D. Chen, J. Zhu, X. Mu, R. Cheng, W. Li, S. Liu, Z. Pu, C. Lin and S. Mu, *Appl. Catal. B: Environ.*, 2020, **268**, 118729.

53. Z. Li, W. Niu, Z. Yang, N. Zaman, W. Samarakoon, M. Wang, A. Kara, M. Lucero, M. V. Vyas, H. Cao, H. Zhou, G. E. Sterbinsky, Z. Feng, Y. Du and Y. Yang, *Energy Environ. Sci.*, 2020, **13**, 884-895.